Hadi Nazaripoor, Charles R. Koch, and Mohtada Sadrzadeh. Ordered high aspect ratio nanopillar formation based on electrical and thermal reflowing of prepatterned thin films. *Journal of Colloid and Interface Science*, 530:312–320, 2018. ISSN 0021-9797. doi: https://doi.org/10.1016/j.jcis.2018.06.080

Journal of Colloid and Interface Science 530 (2018) 312–320

Contents lists available at ScienceDirect

Journal of Colloid and Interface Science

journal homepage: www.elsevier.com/locate/jcis

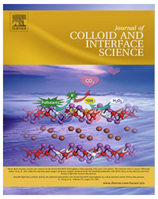

Regular Article

Ordered high aspect ratio nanopillar formation based on electrical and thermal reflowing of prepatterned thin films

Hadi Nazaripoor, Charles R. Koch, Mohtada Sadrzadeh *

Advanced Water Research Lab (AWRL), Department of Mechanical Engineering, 10-367 Donadeo Innovation Center for Engineering, University of Alberta, Edmonton, Alberta, T6G 1H9, Canada

GRAPHICAL ABSTRACT

EIP-TIP reflowing of prepatterned nanofilm to creat werll-ordered and high aspect ration structures

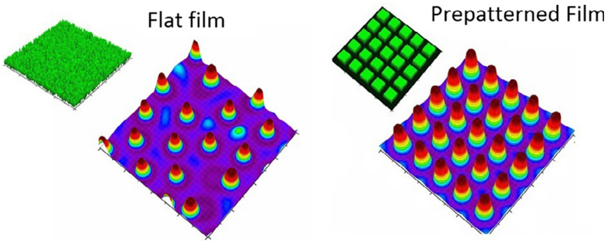

ARTICLE INFO

Article history:
Received 24 May 2018
Revised 25 June 2018
Accepted 26 June 2018
Available online 30 June 2018

Keywords:
Electrohydrodynamics
Thermocapillary
Instability
Thin film
Microfabrication
Nanofabrication

ABSTRACT

Creating well-ordered, submicron-sized pillars have been stated as main limitation for electrically induced patterning of nanofilms (thickness <100 nm) [1]. In our previous works, it was shown that the aspect ratio of formed nanopillars was increased to about 0.35 when thermocapillary induced instabilities (Thermally Induced Patterning, TIP) is combined with electrodynamics instabilities (Electrically Induced Patterning, EIP). However, further reduction of pillar size resulted in a coarse and randomly distributed pillars [2,3]. Here, the reflowing of initially prepatterned nanofilms are examined in the EIP and combined EIP-TIP process to create a well-ordered and high aspect ratio nanopillar arrays without sacrificing the fidelity of the final structure. The long-wave approximation is used to simplify the governing equations and boundary conditions leading to a fourth order nonlinear partial differential equation called *thin film* equation that describes the spatio-temporal evolution of the interface. The mechanism of pattern reflowing is discussed for both linear (initial) and nonlinear (long-term) deformations in EIP and EIP-TIP process. The optimum initial pattern width, height and the center-to-center distance is found based on the characteristic wavelength for growth of instabilities predicted by linear stability analysis and nonlinear simulation results.

1. Introduction

Growing demand for straightforward and cost-effective lithography technique to fabricate micro-/nano structures has led to an intense research in fabrication techniques [4–7]. Making smaller structures with enhanced material properties is one main objective for this research for many applications such as opto-electronic devices, sensors and transistors, micro-/nanofluidic systems. More recently, soft lithography and most importantly contact-less patterning techniques, relies on the self-organization of a liquid (molten polymer) layers [8,9,5,10,7]. Electrically Induced

---

* Corresponding author.
E-mail address: sadrzade@ualberta.ca (M. Sadrzadeh).

https://doi.org/10.1016/j.jcis.2018.06.080
0021-9797/© 2018 Elsevier Inc. All rights reserved.

Patterning (EIP) [11,4] and Thermally Induced Patterning (TIP) [12–15] has emerged as an inexpensive and a straightforward alternative lithography technique for mico-/nanostructing of either conducting and/or non-conducting polymers.

In the EIP, applying an electric field and the difference between the electrostatic properties of liquid film and the bounding layer (the layer which fills the gap between the liquid film and top electrode) results in a net electrostatic (ES) force applied to the interface [16]. The ES force destabilizes the liquid film whereas the viscous force and the Laplace pressure (due to interfacial tension) tend to damp the induced instabilities by the ES force. When the ES force overcomes these damping forces the instabilities grow and the interface reaches to the top electrode to bridge the gap by forming columnar structures called pillars. In the TIP process, a thin liquid film is heated from below and cooled from the top that leads to a large thermal gradient across the micro and nano-sized film. The thermocapillary (TC) force is generated along the interface as the interfacial tension decreases with increasing temperature along the interface. The non-uniformity in the interfacial tension at the interface exerts TC force tangent to the interface which, consequently, leads to a pattern evolution. In ultra-thin (nanofilms) and highly viscous films, the resulting TC instabilities have a large wavelength that leads to motion in the interface. Similarly, it is seen that the instabilities evolve until the columnar structures form and then bridge between the two plates [13–15].

Feature size, aspect ratio (height to width ratio) and their distribution (i.e either randomly distributed or well-ordered) are the main objectives in both EIP and TIP techniques. There have been tremendous efforts to improve pattern formation process, mostly in the EIP, since the initial observation of nanopillar formation in late 1990s [11,12]. The efforts in EIP can be divided into two main streams. One, is working on the electrohydrodynamic (EHD) instabilities in ultra-thin (thickness $\ll 1\ \mu$m). These are mostly focused on: lowering the pillar size to sub-micron level by various means such as enhancing the electrical properties of liquid film [17–19]; lowering the size of system (electrodes distance of 200 nm and less) and applying high electric field; lowering the interfacial tension by introducing bounding layers other than air [20,21]; and using patterned top electrode as mask to replicate features smaller than the characteristic length predicted by linear stability (LS) analysis [22–25]. There has been limitations in lowering the lateral size of pillars as electric break down of either polymer or bounding layer [26,1] which leads to imperfect pattern formation and impedes creating pillars with aspect ratios (ratio of pillar height to its width) greater than one. In the second stream the EIP process, micopillars formed using much thicker films (initial thickness of a few to hundreds microns) by exposing the film to extra high electric field [27,28]. Very recently, it was shown that electrically induced reflowing of a prepattern films results in very high aspect ratio of pillars (aspect ratio: 3–5) [29,27,30]. Since the initial pattern has a very low aspect ratio (height to width), it can be fabricated either using conventional photolithography or hot embossing [29].

In our previous works, we showed that the combination of EHD and TC instabilities will lead to much smaller sized patterns compared to the EIP and TIP formed patterns [2]. However, the presence of tangential TC forces leads to a higher tendency to merge and make larger size pillars which lowers the efficiency of EIP-TIP process [3]. In this study, for the first time, we focus on reflowing "prepatterned nanofilms" using EIP, TIP and combined EIP-TIP process to investigate the capability of this technique in minimizing the pillars size (increasing aspect ratio) and a well-ordered patterns output. The feasibility of using prepatterned nanofilms will be addressed in the following steps: First the effect of (i) initial pattern shape (cubic or spherical-cap protrusions) (ii) height, width and periodicity on the reflowing mechanism (early stages of deformation) and final formed patterns (nonlinear stages) are discussed. Second, finding a threshold value for the initial protrusion height that required to create well-ordered nanopillars. Third, the effect of applied voltage on creating well ordered and high aspect ratio pillars when using prepatterned film in the EIP-TIP process is investigated. Fourth, finding the limitation for the size of initial patterns which either leads to well ordered and high aspect ratio nanopillars or over time damped and re-organized into a coarse structure with larger sized pillars.

2. Mathematical model

A schematic of the EIP, TIP and EIP-TIP process where an ultra-thin liquid film with either intially flat or a prepatterned shape is shown in Fig. 1. Transverse electric field exposed to the film induces *Maxwell* stress normal the film interface due to mismatch of electrical properties of liquid film and the bounding fluid. The transverse thermal gradient is adjusted by heating the film from below (T_h) while keeping the top plate temperature still above glass transition temperature (T_g) but cooler than the lower substrate ($T_h > T_c > T_g$). The tangential TC stress is resulted due to thermal gradient along the interface and the resulting interfacial tension non-uniformity. Interfacial tension approximated to be a linear [31] function of temperature ($\gamma = \gamma_0 - \alpha_T(T - T_0)$) with $\alpha_T > 0$ as the surface tension gradient, γ_0 and T_0 are the reference interfacial tension and temperature. Initially, the interface is considered a flat film (unless it has been prepatterned) as the interface only affected by Brownian motion whose amplitude is negligible compared to the initial thickness of film.

The liquid film is considered as incompressible and Newtonian fluid. Mass conservation, momentum and energy balances governs the dynamics and pattern formation process. Considering the long-wave approximation, the spatio-temporal evolution of thin liquid films subjected to the transverse electric field and thermal gradient is described by the following dimensionless equation [32],

$$\frac{\partial H}{\partial \tau} + \nabla.\left(H^3 \nabla P - \frac{3H^2}{2} \nabla \Gamma\right) = 0 \qquad (1)$$

where $H = H(X, Y, \tau)$ is nondimensional interface height that is a function of lateral coordinates X, Y and time τ, and $\nabla = (\partial/\partial X, \partial/\partial Y)$. The horizontal coordinates are normalized with characteristic wave-length of $l_c (X, Y = x/l_c, y/l_c)$. The vertical coordinate, interface height and electrodes distance is scaled with film initial thickness h_0 ($Z = z/h_0, H = h/h_0$ and $D = d/h_0$) and temperature is normalized as $\theta = (T - T_c)/(T_h - T_c)$. Variable $\epsilon\ (= h_0/l_c) \ll 1$ is the dimensionless ratio of initial film thickness to the characteristic lateral length scale which confirms the validity of long-wave

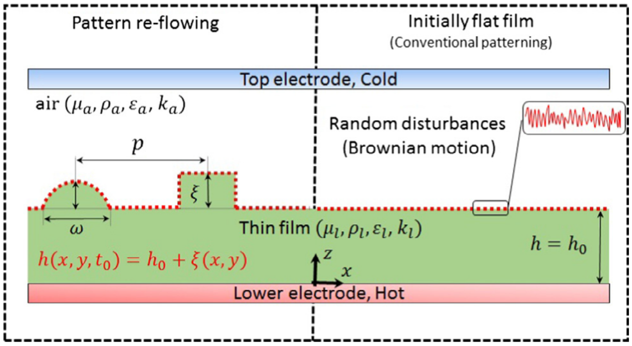

Fig. 1. A 2D schematic of EIP-TIP process. The ultra-thin prepatterned film is sandwiched between top (cold) and bottom (hot) electrodes. Initial height profile in prepatterned film is $h(x, y, t_0) = h_0 + \xi(x, y)$. p is center-to-center distance, ξ is height and w is width of protrusions.

approximation. Dimensionless time is $\tau = (3u_c/l_c)t$ and u_c is the characteristic lateral speed due to either individual TC and EHD flow or their combination [14]. The film density $\rho = \rho(T_h)$ and viscosity $\mu = \mu(T_h)$ are assumed constant. The dielectric constant of polymer films varies at non-isothermal condition [33,34]. In this study it is assumed the variation in the dielectric constant of polymer film is negligible and does not vary by temperature.

The second term in (1), shows the superposition effect in the growth of instabilities and change in the interface height due to variations in normal (hydrostatic) forces ∇P and tangential TC force $\nabla\Gamma = (d\Gamma/d\theta)\nabla\theta_{(Z=H)}$. Term $\nabla\theta_{(Z=H)}$ refers to the gradient of temperature at the interface. The variable $\Gamma = (\epsilon h_0/\mu u_c)\gamma$ is the dimensionless interfacial tension and $P = \epsilon h_0/\mu u_c(p+\phi)$ is the dimensionless pressure in which p represents the capillary pressure and $\phi = -\rho gz + \phi_{LW} + \phi_{ES}$ is for the contributions of hydrostatic pressure, Lifshitz-Van der Waals intermolecular interactions and ES pressure [32].

Lifshitz-Van der Waals intermolecular interactions $\phi_{LW} = -A/(6\pi H^3)$ are also considered in this study as the film thickness is less than 1 µm. Variable A is the effective Hamaker constant defined for the three layer system $(A = (\sqrt{A_a} - \sqrt{A_l})(\sqrt{A_s} - \sqrt{A_l}))$ where A_l, A_a and A_s is Hamaker constant of the liquid film, air and substrate, respectively [35]. The electrostatic component of *Maxwell* stress acting on the film interface $\overline{M} = \varepsilon\mathbf{EE} - 0.5\varepsilon\mathbf{E}\cdot\mathbf{E}\bar{I}$, depends on the electric field, $\mathbf{E} = -\nabla\psi$, in each layer. Electric potential ψ_i, in each layer ($i = 1,2$ for liquid film and air layer) is found by solving Poisson equation $\nabla^2\psi_i = -\rho_e/\varepsilon_i$. In perfect dielectrics, the term ρ_e which is the free charge density vanishes and ε is the dielectric constant of layer. The resulting net ES pressure in the long-wave limit is found as,

$$\phi_{ES} = -0.5\varepsilon_l(\varepsilon_r - 1)\left[\frac{\Delta\psi}{(\varepsilon_r - 1)h - \varepsilon_r d}\right]^2 \tag{2}$$

where $\varepsilon_r = \varepsilon_l/\varepsilon_a$ is the relative dielectric constant of film to the air bounding layer. Given these, the hydrostatic term in (1) becomes,

$$\nabla P = Ca^{-1}\nabla^3 H - Ca^{-1}Bo\nabla H + \nabla(\Phi_{LW} + \Phi_{ES}) \tag{3}$$

where, Capillary number $Ca = \mu u_c/(\epsilon^3\gamma)$ and Bond number $Bo = \rho g l_c^2/\gamma$ and Φ_{LW}, Φ_{ES} are dimensionless Lifshitz van der Waals and ES pressures.

In order to find the TC tangential force acting on the interface which is related to the interfacial tension gradient $\nabla\Gamma$ and thermal gradient along the interface, the energy balance equation is solved in its long-wave limit form. As the film thickness is in range of submicron level the heat conduction is found as the dominant mode of heat transfer compared to convection, the Biot number $Bi(= h_f h_c/k) \ll 1$ in which h_f is the film thickness and h_c is convective heat transfer coefficient and k is the thermal conductivity of the film. The temperature distribution along the interface is $\theta|_{Z=H} = k_r(D-H)/[(1-k_r)H - +k_r D]$ where $k_r = k_l/k_a$ is the relative thermal conductivity of layers. Substituting this into TC pressure term yields,

$$\nabla\Gamma = \frac{k_r D Ma}{[(1-k_r)H + k_r D]^2}\nabla H \tag{4}$$

where, $Ma = \epsilon\alpha_T\Delta T/(\mu u_c)$ is the Marangoni number and $\Delta T = T_h - T_c$ is the maximum temperature difference.

Substituting of (3) and (4) into (1) then yields to the thin film equation which governs the spatio-temporal evolution of film under EHD and TC instabilities.

$$\frac{\partial H}{\partial\tau} + \nabla.\left(H^3\left[Ca^{-1}\nabla_{\parallel}^3 H - Ca^{-1}Bo\nabla H - \nabla(\Phi_{LW} + \Phi_{ES})\right] - H^2\nabla\Gamma\right) = 0 \tag{5}$$

This is the general form of thin film equation under both electrical and thermal gradient. In 5, the contributions of gravity to the hydrostatic pressure are neglected compared to other forces as the experimental work of EHD and TC of ultra-thin liquid (thickness $< 1\mu m$) films [36,37,14,15], have a Capillary number and Bond number that are of the order of $O(1)$ and $O(-5)$. In the derivation of Eq. (5), it is assumed that: (i) there is no electric breakdown in both liquid film and the bounding layer, (ii) the solvent evaporation is completed before the onset of TC and EHD patterning process and (iii) the liquid film viscosity (molten polymer at a temperature above the glass transition $T > T_g$) is constant over the evolution time.

2.1. Scaling and numerical scheme

With no applied electric field ($\Delta\psi = 0$), the TC is dominant in heated films, both viscous scaling (current version of Eq. (5)) [14,15] and LW scaling [31,38] have been used to normalize the TC pressure. In the electrically induced instabilities under isothermal condition, the ES pressure considered as dominant [36,39] then Eq. (5) is re-scaled using factors of $L_s = (\gamma h_0^3/0.5\varepsilon_r(\varepsilon_r - 1)\Delta\psi^2)^{\frac{1}{2}}$, $T_s = 3\mu\gamma h_0^3/[0.5\varepsilon_r(\varepsilon_r - 1)\Delta\psi^2]$ and $\Phi_s = 0.5\varepsilon_r(\varepsilon_r - 1)(\Delta\psi/h_0)^2$.

The re-scaled thin film equation is then numerically solved to study the dynamics and pattern evolution on the liquid film. First, the spatial derivatives ($\frac{\partial}{\partial x}$ and $\frac{\partial}{\partial y}$) are discretized using finite difference scheme, then, the resulting system of ordinary differential equations (ODE's) in time are solved using an adaptive time step solver of DASSL [40]. Periodic lateral boundary condition is used for an square computational domain with size of $16\lambda^2$. The parameter λ is set to either equal to or a fraction ($\beta \leq 1$) of the scaled characteristic wavelength for growth of instabilities predicted by LS analysis, $\lambda = \beta(\Lambda_{LS}/L_s)$. The initial condition of the film is conventionally considered to be flat and the deformation started from initial random perturbation (with very small amplitude, $\widehat{\xi}$) of the film while conserving its volume. In this study a random perturbation with very small amplitude compared to height of the initial film pattern ($\widehat{\xi}/\xi \ll 1$) or an initial prepatterned film to investigate the pattern reflowing in EIP and combined EIP-TIP process is used. The characteristic wavelength for growth of instabilities using LS analysis is reported for the EIP-TIP process [2,3] as

$$\frac{\Lambda_{LS}}{L_s} = 2\pi\left[\frac{\varepsilon_r - 1}{[1 + \varepsilon_r(D-1)]^3} + \frac{\overline{Ma}k_r D}{[1 + k_r(D-1)]^2}\right]^{-\frac{1}{2}} \tag{6}$$

where modified Marangoni number $\overline{Ma} = 3\alpha_T\Delta T/(2h_0\Phi_s)$ shows the relative strength of interfacial force gradient to the ES force. The Λ_{LS} for the case of EIP ($\Delta T = 0$) in Eq. (6) is named as Λ_{LSE}. Constants and parameters used in this study are presented in Table 1.

Table 1
List of constants and parameters used in the modeling.

Parameter	Value
Viscosity of liquid film (μ_l)	1 [Pa s]
Interfacial tension (γ)	0.048 $\left[\frac{N}{m}\right]$
Interfacial tension gradient (α_T)	48×10^{-5} $\left[\frac{N}{m\,^\circ C}\right]$
Effective Hamaker constant (A)	-1.5×10^{-21} [J]
Vacuum dielectric constant (ε_0)	8.85×10^{-12} $\left[\frac{C}{V\,m}\right]$
Dielectric constant of the liquid film (ε_l)	$2.5 \times \varepsilon_0$ $\left[\frac{C}{V\,m}\right]$
Dielectric constant of the air (ε_a)	$1 \times \varepsilon_0$ $\left[\frac{C}{V\,m}\right]$
Initial film thickness (h_0)	20–70 [nm]
Electrodes distance (d)	400 [nm]
Equilibrium distance (l_0)	2–5 [nm]
Temperature difference (ΔT)	0–100 [°C]
Applied voltage ($\Delta\psi$)	0–300 [V]

3. Results and discussion

3.1. Combined EIP-TIP and initially flat film (base-case)

The addition of TC force to the electrically induced instabilities results in smaller sized features compared to the EHD induced patterning [2,3]. The LS analysis predictions also showed that the Λ_{LS} can be lowered by a factor of three in the combined EIP-TIP process. However, the tangential TC force accelerates the coarsening stage and the pillars start to merge in early stages of deformation resulting in larger sized features. The merging of pillars at early stages significantly affects the shape and size of final pattern leading to a significant deviation from LS analysis predictions. This deviation is found to be insignificant in EIP process at micron-sized patterns. As a base-case, the spatio-temporal evolution of a 60 nm film under the combined EHD-TC condition is studied and results are presented in Fig. 2. The film considered is initially flat and instabilities are growing from very small amplitude of random perturbation. The maximum and minimum interface height is tracked over time (image (a)) to show the progress in growing instabilities and steps in pillar formation. Time evolution of the pattern formation are presented by the 3D snapshots of the interface profile that shows: the (i) initial reorganization of instabilities and ridge and valleys formation (image b(i) and b(ii)) fragmentation and isolated pillar formation (image b(ii) and b(iii)) completion of first pillar formation which bridge the top and bottom plates which is followed by pillar formation in other areas (image b(iii) and b(iv)) beginning of the coarsening stage mixed with completion in pillar formation (image b(iv) and b(v)) coarsening stage which pillars merge to form larger size pillars (image b(v) and b(vi)) quasi-steady stage of formed patterns in EIP-TIP process. Although the nonlinear numerical simulations showed pillar's lateral size is still in submicron level, as seen in image b(v) and b(vi), they are randomly distributed and did not follow the conventional hexagonal pattern observed in the EIP.

The prepatterned film has been introduced in the EIP process to control the pillar's location and increasing their aspect ratio (pillars height to width) for micron sized film [27,29,30]. However, the possibility of using prepattern nanofilms to create well-ordered nanopillars with high aspect ratio using EIP and EIP-TIP has not been explored. In what follows, the reflowing mechanism for prepatterned nanofilms, the effect of initial pattern size and shape and the role of TC increasing high aspect ratio pillars will be discussed.

3.2. Prepatterned film: EIP-TIP vs. EIP

Two initial shape of square block and spherical-cap shape protrusions are used to study the reflowing in prepatterned nanofilms. The height of protrusion is ξ, the width is w and their center-to-center distance is p (shown in Fig. 1) and they are normalized by initial base thickness of h_0 and lateral scaling factor of L_s, respectively for the nonlinear analysis. The 3D snapshots for pattern formed at initial stage of EIP and EIP-TIP process using two initial shape of square block and spherical-cap shape protrusions are shown in Fig. 3. The domain size is selected based on the EIP characteristic wavelength to compare the EIP-TIP and EIP under the same initial condition. The protrusion height and width in square block shape and the spherical-cap protrusions is set $\xi = 0.1h_0$ and $w = \Lambda_{LSE}$, respectively.

From Eqs. (2) and (4), the film interface experiences higher ES and TC pressure at the protruded area. Therefore, the reflowing of the initial pattern toward the top electrode begins with the protruded area with higher initial thicknesses, then it extends to other regions. Irrespective of the initial shape of pattern, either square

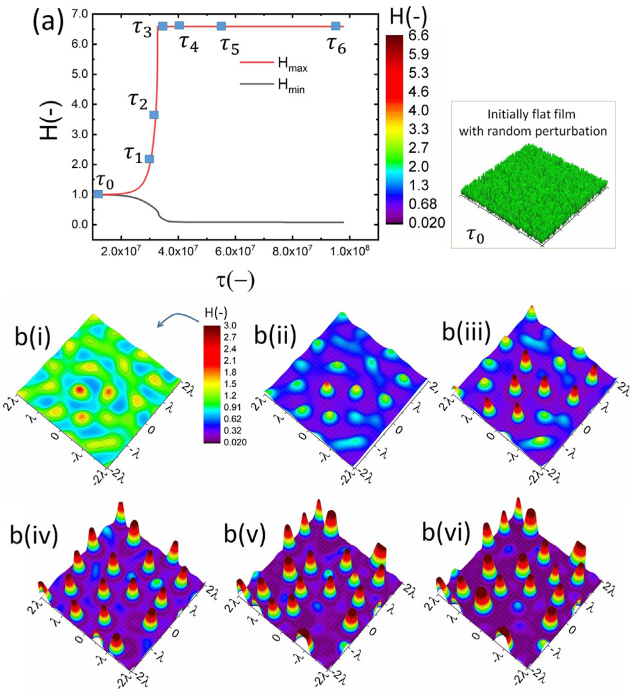

Fig. 2. (a) Tracking the maximum and minimum interface height over time and b(i–vi) 3D snapshots of the interface in EIP-TIP process using initially flat film. Nondimensional times ($\tau(-) \times 10^{-7}$): b(i) τ_1 =3.0, b(ii) τ_2 =3.2, b(iii) τ_3 =3.4, b(iv) τ_4 =4.0, b(v) τ_5 =5.47, b(vi) τ_6 =9.5. $\xi = 0, w = \Lambda_{LS}, \beta = 1, h_0$ =60 nm, d =400 nm, $\Delta\psi$ =300 V, ΔT = 100 °C.

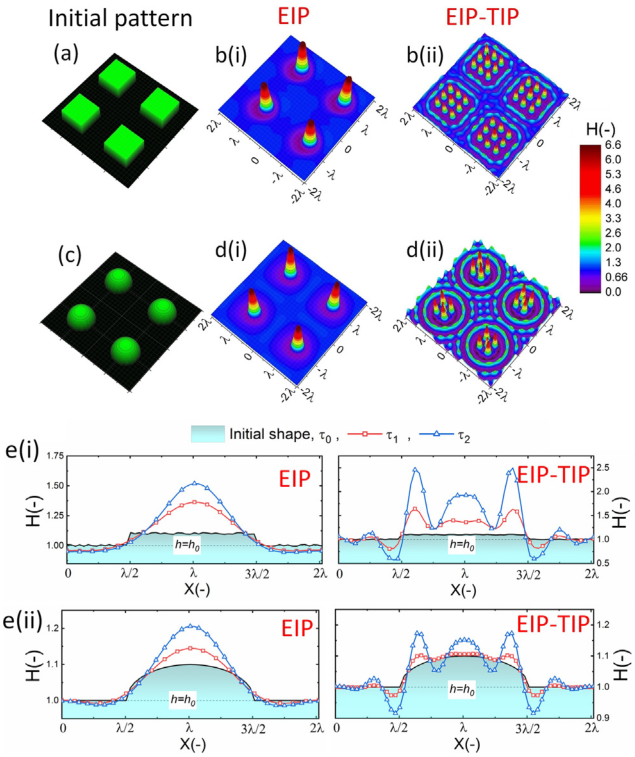

Fig. 3. 3D snapshots (a–d) and 2D height profiles (e) of the interface in EIP and EIP-TIP process. Nondimensional time ($\tau(-) \times 10^{-5}$): b(i) 132.5, b(ii) 2.35, d(i)128.3, d(ii) 1.5, e(i) EIP: $\tau_1 = 8.65, \tau_2 = 70.78$ and EIP-TIP: τ_1 =1.03, τ_2 =1.56 and e(ii) EIP: τ_1 =13.21, τ_2 =30.39 and EIP-TIP: τ_1 =0.521, τ_2 =1.02. $\xi = 0.1h_0, w = \Lambda_{LSE}, \beta = 1$, h_0 =60 nm, d =400 nm, $\Delta\psi$ =50 V, ΔT = 100 °C.

block or spherical-cap protrusion, only one pillar formed from each protrusion in the EIP case (compare image b(i) and image d(i) in Fig. 3). However, in the EIP-TIP case, the initial shape of the protrusion affects both the resulting pattern and the pillars distribution (compare image b(ii) and image d(ii) in Fig. 3). For the square block case, the wavelength grows in lateral (X and Y) direction parallel to the initial pattern walls ($\tau = \tau_0$) and results in formation of 9 pillars at the protruded area. However, in the spherical cap pattern, the instabilities grow in circular concentric wave form leading to formation of five pillars at the protruded area.

To further explore the reflowing mechanism, the early stages of pattern formation using square shape prepatterned films are compared for EIP and EIP-TIP process in images e(i) and e(ii). The difference between EIP and EIP-TIP later using prepatterned film starts at very early stages of pattern formation ($\tau = \tau_1$). In the EIP, the interface is pulled toward top electrode at the center of protrusion ($X = \lambda$) whereas in the EIP-TIP the initial perturbations amplified around the edge of the protrusion where ES and TC forces have higher gradient ($X = 0.5\lambda$ and 1.5λ). When using prepatterned film, both ES and TC forces show a jump in their magnitude with the highest gradient right at the edges. In the case of EIP, this abrupt change in ES force around the edges exists but it is mostly damped by the Laplace pressure (due to high curvature of the film) at early stages. It must be noted that, the ES force acts normal to the interface, while the TC force acts in the tangential direction. Hence in the combined case of EIP-TIP, the presence of TC tangential force leads to a higher growth in instabilities around the edges in addition to the ES force induced instabilities. The pattern formation using the spherical-cap shape is found to be complex compared to the square block or a rectangular shape, so the complete spatio-temporal evolution of the film interface in the EIP-TIP case using spherical-cap protrusion is discussed (Section 1. in electronic supporting materials).

3.3. EIP-TIP in prepatterned film: effect of protrusion height

In Fig. 3, the resulting pattern in EIP-TIP is found to be sensitive to the initial shape of interface compared to the EIP where the height of the protrusion used was relatively small compared to the base thickness ($\xi = 0.1h_0$). The effect of height of the protrusion on the ES and TC pressures are presented in Fig. 4(a). The relative height of protrusion is ξ/h_0 since the interface height $h(x, y, t)$ is scaled with the base initial film thickness of h_0. The ES and TC pressures are normalized with the ES and TC pressure acting on the non-protruded area ($\phi^* = \phi/\phi_{h_0}$). As the ξ/h_0 increases both the ES (ϕ^*_{ES}) and TC (ϕ^*_{TC}) pressure increases on the protruded area (see image (a)) resulting to higher gradient in net force around the edges. The effect of ξ/h_0 on the pressure applied to the interface is found to be more significant when the liquid film has higher relative electrical (ε_r) and thermal (k_r) conductivity compared the bounding layer and when the relative height of the protrusion is $\xi/h_0 \geqslant 2$. Figs. 4b(i)–b(iv) shows the initial stage of pattern reflowing for square block prepatterned films with relative block height of $\xi/h_0 = 0.1, 0.5, 2$ and 4. These nonlinear simulation results show that increasing the height of the protrusions lead to a single columnar structure forming whereas in the smaller ξ/h_0 values mutliscale patterns formed. Increasing the ξ/h_0 leads to a lower number of pillars forming at the protruded region which are less stable with a higher tendency to merge in later stages (results are not shown here).

When the height of initial pattern is very small ($\xi/h_0 = 0.1$ and 0.5), using the prepattern film mostly affects the pillars distribution as the initial deformation on the protruded area merge with the base layer and after that the spatiotemporal evolution follows similar steps observed for an initially flat film. Also, the propagating waves (on non-patterned area) follow the initial shape of protrusions and pillars form along the propagating waves that leads to a well ordered pattern (also shown at Section 1 in the electronic supporting information). Increasing the initial protrusion height ($\xi/h_0 = 2$ and 4) results in having enough polymer mass to reach to the top plate at earlier times that leads to the formation of larger size pillars bridging the gap above the protruded area.

So far understanding the dynamics and reflowing of prepatterned nanofilms in EIP and EIP-TIP process and showing that the increase in the initial height of pattern leads to a different morphological evolution steps and consequently different features forming in nanofilms has been the focus. Next, the effect of protrusion width and their center-to-center distance on the pattern reflowing in the EIP and EIP-TIP process will be discussed.

3.4. EIP-TIP in prepatterned film: effect of protrusion width

The protrusion width is decreased from Λ_{ES} to $(2/3)\Lambda_{ES}$ and the center-to-center distance is decreased from $2\Lambda_{ES}$ to $(4/3)\Lambda_{ES}$. Based on the new pattern dimensions, under the same domain area ($\beta = 1$), the prepattern film has 9 square block protrusions in $16\lambda^2$ domain. The reflowing mechanism and the spatio-temporal morphologies of the film interface under EIP process are shown in Fig. 5. The initial height of the protrusions is set to $\xi = 2h_0$. The maximum interface height shows a gradual increase at early

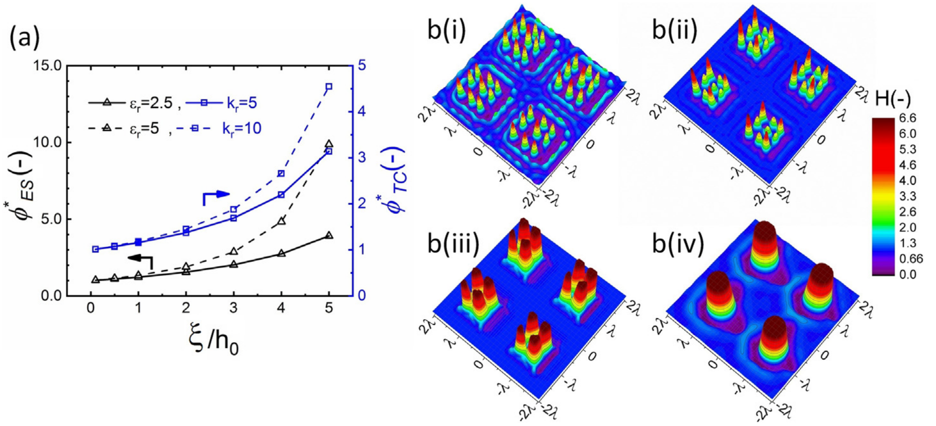

Fig. 4. EIP-TIP process and four square block protrusions. (a) Normalized ES pressure (ϕ^*_{ES}, left axis) and TC pressure (ϕ^*_{TC}, right axis) variations versus relative protrusion's heights ξ/h_0 for two relative electric permittivity and thermal conductivity ratios. 3D snapshots of the interface morphology resulting from a square block prepatterned film and relative height of $\xi/h_0 =$ b(i) 0.1, b(ii) 0.5, b(iii) 2 and b(iv) 4. $\beta = 1$,$w = \Lambda_{LSE}, p = 2w, h_0 =$60 nm, $d =$400 nm, $\Delta\psi =$50 V, $\Delta T = 100$ °C.

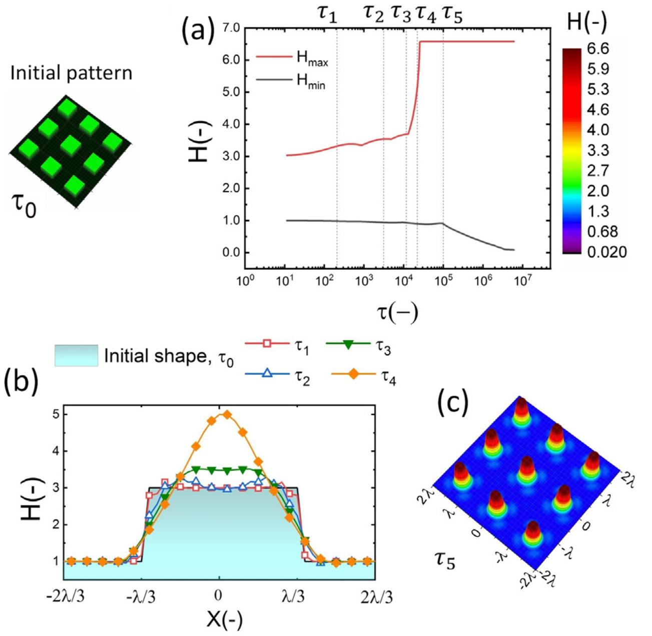

Fig. 5. (a) Tracking the maximum and minimum interface height over time, (b) 2D height profile at early stages of the pattern reflowing and (c) 3D snapshot of the interface morphology at quasi-steady state. Nondimensional times ($\tau(-)$): $\tau_1 = 209$, $\tau_2 = 3154$, $\tau_3 = 11680$, $\tau_4 = 22083$, $\tau_5 = 100275$. $\xi = 2h_0, w = 2\Lambda_{LS}/3, p = 4\Lambda_{LS}/3, \beta = 1, h_0 = 60$ nm, $d = 400$ nm, $\Delta\psi = 300$ V, $\Delta T = 0$ °C.

stages of deformation (from τ_1 to τ_3) as the initial pattern is deforming from the square to pillar structure. Similar to the cases showed in Fig. 3 e(i) for wider and smaller sized protrusions, the initial deformations around the edges merge to form only one pillar. Over time the formed pillar grows and touch the top electrode and are well ordered and have the aspect ratio of 0.15. To decrease the pillar width to submicrom level and increase their aspect ratio, the initial pattern width and the center-to-center distance is further decreased to $w = \Lambda_{ES}/3$ and $p = 2\Lambda_{ES}/3$.

The reflowing mechanism and the spatio-temporal morphologies of the film under EIP and EIP-TIP process for the reduced size prepatterned film are compared in Fig. 6. The initial height of the protrusions is kept the same as before ($\xi = 2h_0$). Tracking the maximum interface height in both EIP and EIP-TIP process shows an abrupt increase in the height at very early stages of pattern reflowing (τ_0). This initial reforming is found visible when the initial pattern size is lowered and leads to very high surface to volume ratio for the initial square blocks. Since the deformation from square block to a pillar shape happened at very early stages of the process, the pattern reforming occurred under a constant volume of fluid and it is mainly due to a large Laplace pressure acting on the interface tending to minimize the surface area. In the EIP case (image 6 (a)), the initial jump is damped and the H_{max} has a gradual decrease over time until it reaches the initial height.

The 3D snapshot at later stage (τ_1) shows only the pillar located at the center grows to touch the top electrode (image 6 a(iii), τ_2). Other lateral pillars, first moved away from the center and then reached to the top electrode (image 6 a(iv) and a(v), τ_3 and τ_4). This results in an increase in the center-to-center distance of formed pillars to $p = 2\Lambda_{ES}$ at the final formed pattern in the EIP process. At this stage, pillars are similar in size and equally spaced (similar center-to-center distance) and have a symmetric pattern. Therefore, pillars do not tend to merge, and the resulting pattern remains stable for a long time. Hence, pillars do not tend to merge that leads to a quasi-steady stage condition and making a stable pattern formation. The EIP-TIP process is also examined under the same initial condition which results are shown in Fig. 6(b). At initial stage, τ_0, similar to the EIP case, there is a jump in the interface height that represents the reflowing from square block to columnar shape structure. Note that the time axis is plotted in log scale so an abrupt increase in height is not present. Over time, the height of the pillars increase and pillars touch the top electrode. In contrast to the EIP case, in the EIP-TIP all pillars are grown toward top electrode with no lateral movement leading to 9 pillars

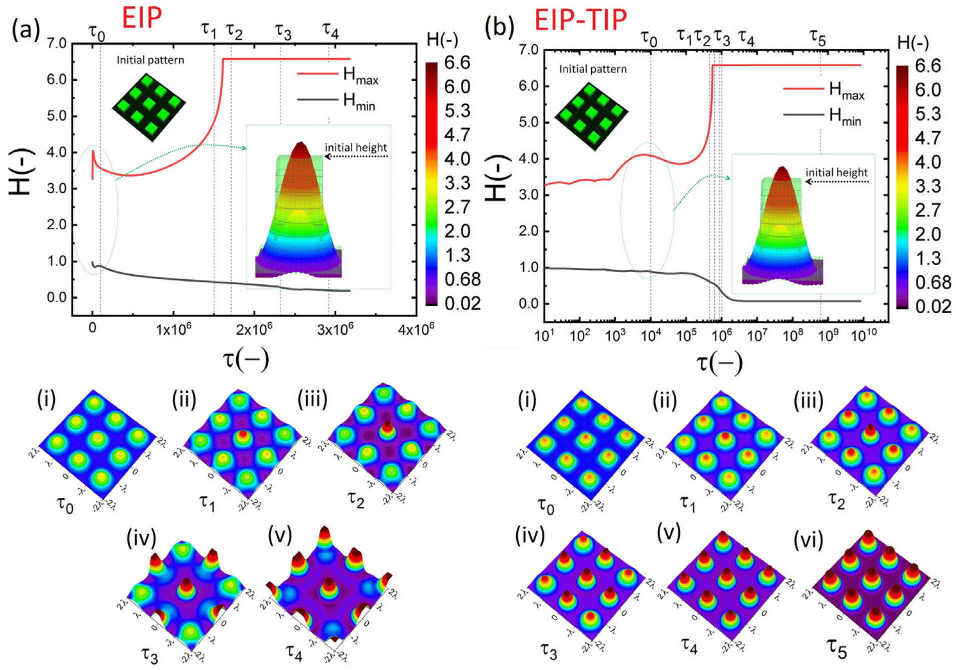

Fig. 6. Tracking the maximum and minimum interface height over time and 3D snapshots of the interface in (a) EIP and (b) EIP-TIP process using initially prepatterned film. Nondimensional times ($\tau(-) \times 10^{-6}$): a(i) $\tau_0 = 0.1$, a(ii) $\tau_1 = 1.5$, a(iii) $\tau_2 = 1.7$, a(iv) $\tau_3 = 2.3$, a(v) $\tau_4 = 2.9$ and b(i) $\tau_0 = 0.01$, b(ii) $\tau_1 = 0.46$, b(iii) $\tau_2 = 0.63$, b(iv) $\tau_3 = 0.86$, b(v) $\tau_4 = 1.01$, b(vi) $\tau_6 = 6.2$. $\xi = 2h_0, w = \Lambda_{LS}/3, p = 2\Lambda_{LS}/3, \beta = 0.5, h_0 = 60$ nm, $d = 400$ nm, $\Delta\psi = 300$ V, $\Delta T = 100$ °C.

being formed (image b(iv) and b(v)). The formed pillars are stable for a long time (image 6b(vi)). This shows the addition of TC forces leads to more compact and well ordered structure formation using prepatterned film that is stable in time.

3.5. EIP-TIP in prepatterned film: protrusion width and height interdependence

The effect of relative height of initial pattern is re-examined for a new set of conditions (at reduced protrusion's width $w = \Lambda_{LS}/3, p = 2\Lambda_{LS}/3$ and $\beta = 0.5$). The 2D height profile and 3D snapshots of the structure form on the film are presented in Fig. 7. The relative height ξ/h_0 is varied from 0.1 to 3 and the nonlinear simulations show that based on the relative height of the protrusions two distinct structures formed. The first type is the perfect reflowing of the initially prepatterned film that leads to well-ordered and equal sized pillars (L_1 and image(I)) while the second type is imperfect reflowing in which pillars re-arrange themselves to a higher cenre-to-centre distance. The 2D height profile along L_1 and L_2 in Fig. 7 shows that the pillar formed at the center are identical in both cases, but the lateral pillars larger and more widely spaced in the imperfect reflowing. The minimum protrusion height ($\xi \geqslant 1.5h_0$) is found as the threshold value for the height of the protrusion required to achieve the optimal reflowing and well ordered nanopillars formation.

3.6. EIP-TIP in prepatterned film: high aspect ratio nanopillars

The effect of applied voltage on the resulting pattern and the pillars aspect ratio is also studied for the EIP-TIP process. In Fig. 8(a), the aspect ratio of pillars is found from the nonlinear simulation results. The LS predicted characteristic wavelength for growth of instabilities in the EIP-TIP process are based of Eq. (6). Increasing the applied voltage leads to smaller sized pillars and thus pillars with higher aspect ratios. Despite the parabolic decrease in the Λ_{LS}, the change in aspect ratio of pillars has only a linear increasing trend. In contrast to EIP where only one set of pillars are formed, in EIP-TIP at very low applied voltages (case (i) and (ii)) primary and secondary pillars form. Fig. 8(b)–(d) show the resulting pattern that forms at higher applied voltage ranges.

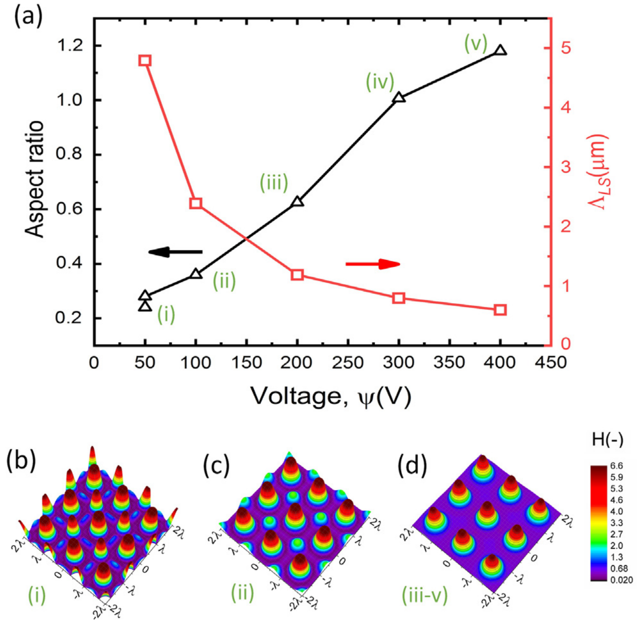

Fig. 8. (a) Effect of applied voltage on the aspect ratio of pillars and the LS predicted characteristic wavelength for growth of instabilities, (b–d) 3D snapshots of the pattern formed predicted by nonlinear analysis in the EIP-TIP and prepatterned nanofilm. $\xi = 2h_0, w = \Lambda_{LS}/3, p = 2\Lambda_{LS}/3, \beta = 0.5, h_0$ =60 nm, d =400 nm and ΔT = 100 °C.

From a thermodynamic point of view, the EIP and EIP-TIP are energy driven processes, and the film evolves until it reaches its minimum energy level (stable condition) [41]. However, the quasi-steady stage is the level, when the formed patterns remain unchanged for an extended period. Merging of pillars to create larger size structures (lower the surface area) mostly happens when homogeneous electric field or uniformly heated films are used. Collision of neighbor pillars and Ostwald ripening are two commonly seen coarsening mechanism in the self-organized patterning techniques (EIP and EIP-TIP). Pillars do not tend to merge for a long period (considered as a quasi-steady stage) when the generated pillars have the same size and their center-to-center distance is the same that leads to the formation of symmetric patterns.

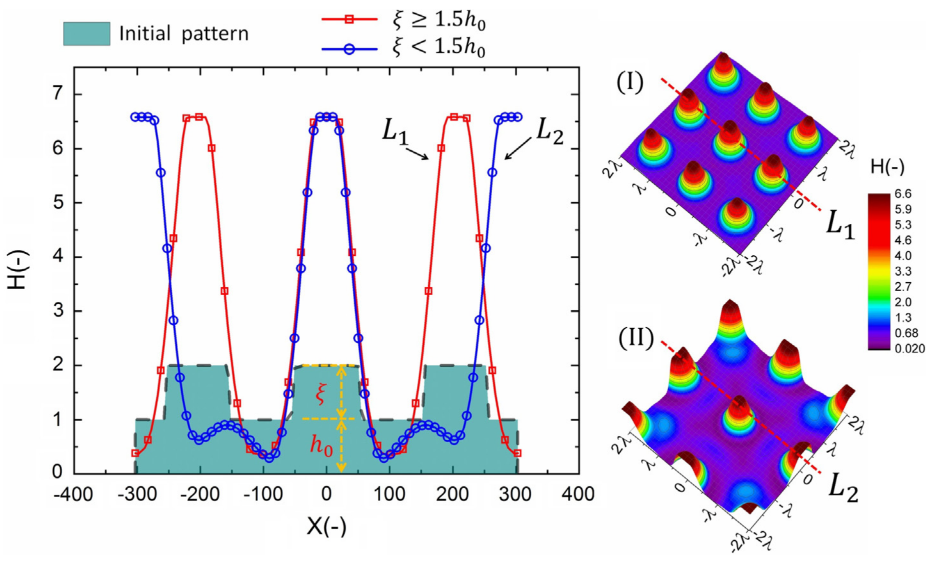

Fig. 7. 2D height profile and 3D snapshots of the pattern forming in the EIP-TIP process, effect of relative height ξ/h_0 at reduced protrusion's width $w = \Lambda_{LS}/3$. Other parameters: $p = 2\Lambda_{LS}/3, \beta = 0.5$. h_0 =60 nm, d =400 nm, $\Delta\psi$ =300 V, ΔT = 100 °C.

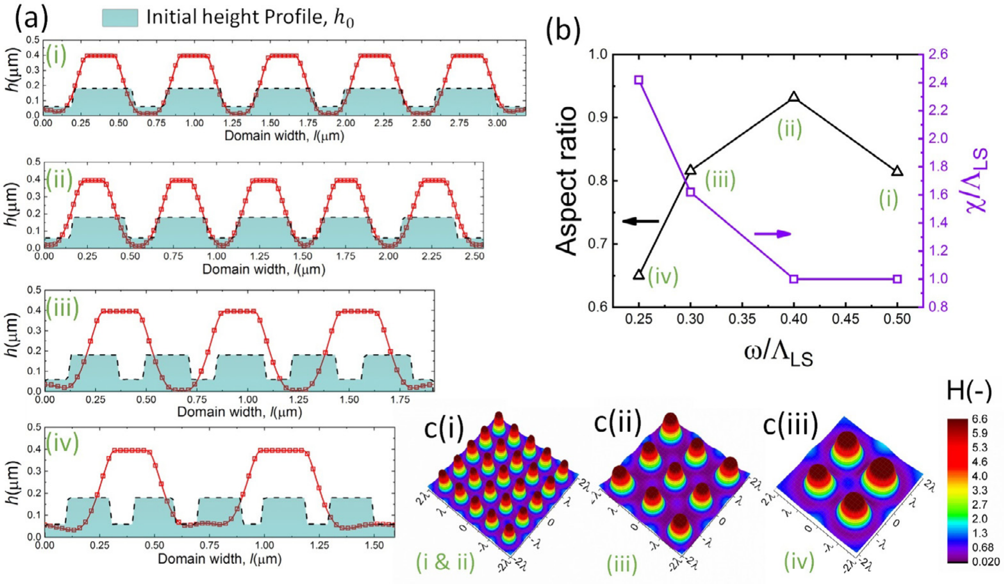

Fig. 9. (a) 2D height profile, (b) aspect ratio and pillars centre-to-cnetre distance and (c) 3D snapshots of the pattern forming at quasi-steady stage in the EIP-TIP process, effect of relative width w/Λ_{LS} for square block protrusions. Other parameters: h_0 =60 nm, d =400 nm, $\Delta\psi$ =300 V, ΔT = 100 °C.

3.7. EIP-TIP in prepatterned film: aspect ratio and limitations

In the previous section, it is shown that ordered pillars with higher aspect ratio can be created by increasing applied voltage. However, due to the electric breakdown limit of polymer film and the bounding layer, the increase in applied voltage is limited. Another option is to lower the spacing and width of initial pattern which the results presented in Fig. 9. The protrusions width and the center-to-center distance is lowered from $w = \Lambda_{LS}/2,\ p = 2\Lambda_{LS}\ \&\ \beta = 1$ to $w = \Lambda_{LS}/4,\ p = \Lambda_{LS}/2\ \&\ \beta = 0.5$. Under this configuration the polymer film is prepatterned with 25 square block protrusions. The 2D height profile at the quasi-steady stage of patterning for 4 different configurations of $w/\Lambda_{LS} = 0.5$, 0.4, 0.3 and 0.25 is shown in image 9 a(i-iv). The aspect ratio and the center-to-center distance of pillars formed (χ/Λ_{LS}) are measured and reported in image 9(b). The 3D profile of the pattern form under these conditions are presented in image 9c(i–iii). Results show that the aspect ratio is increased from 0.81 to 0.93 as the protrusions width (w/Λ_{LS}) decreased from 0.5 to 0.4. In this case, 25 well-ordered nanopillars formed without sacrificing the fidelity of the final structure as χ/Λ_{LS} remained unchanged. However, further decrease in $w/\Lambda_{LS} = 0.3$ and 0.25, results in a coarse structure as only 9 and 4 larger sized pillars having a lower aspect ratio, respectively. The coarse structure $(\chi/\Lambda_{LS} > 1)$ formation is due to merging of square blocks at early stages of reflowing that leads to larger sized pillars at later stages.

4. Conclusions

Creating well-ordered with submicron size pillars have been considered as main limitation for EIP process in nanofilms [1]. Although using patterned top electrode helped to lower the size and create well ordered structures, the very low aspect ratio of formed pillars remained as unsolved problem [22,4,42]. In the EIP process of nanofilms, the aspect ratio of formed pillars was found to be less than 0.2 [39,4] and it was improved to about 0.35 in the EIP-TIP process [2]. But further efforts to lower the pillars width resulted in a coarse and randomly distributed pillars [3]. In this work, the EIP process is combined with TIP to reflow the initially patterned nanofilms and create well-ordered nanopillar arrays with higher aspect ratios.

The feasibility of using prepatterned nanofilms is addressed in the following steps: the effect of (i) initial pattern shape (cubic or spherical-cap protrusions) (ii) height, width and periodicity on the reflowing mechanism (early stages of deformation) and final formed patterns (nonlinear stages) are discussed. Nonlinear analysis showed that despite the EIP process, the EIP-TIP is sensitive to the initial shape of the pattern, even for the small relative protrusion height $(\xi/h_0 = 0.1)$, as the features formed in the nonlinear stages affected by the initial pattern shape. Effect of ξ/h_0 on the ES and TC pressure applied to the interface is significant when the liquid film has higher relative electrical (ε_r) and thermal (k_r) conductivity compared the bounding layer and when the relative height of the protrusion is $\xi/h_0 \geqslant 2$. In addition, increasing the height of the protrusions lead to a single columnar structure forming (with lower aspect ratio) whereas for the smaller ξ/h_0 values hierarchical patterns are formed. However, to have equally-sized pillars and to avoid a multi-scale pattern formation, using $\xi/h_0 \geqslant 2$ is recommended. The effect of protrusions width is also examined on the aspect ratio of pillars and pattern fidelity. The limiting ratio of $w/\Lambda_{LS} = 0.4$ is found as the optimum width ratio as the smaller sized protrusions leads to larger sized pillars with lower aspect ratios. Increasing the applied voltage leads to a smaller sized pillars and thus pillars with higher aspect ratios (around one). Despite the parabolic decrease in the Λ_{LS}, the change in aspect ratio of pillars is found to be only linear.

Appendix A. Supplementary material

Supplementary data associated with this article can be found, in the online version, at https://doi.org/10.1016/j.jcis.2018.06.080.

References

[1] C.Y. Lau, W.B. Russel, Fundamental limitations on ordered electrohydrodynamic patterning, Macromolecules 44 (19) (2011) 7746–7751, https://doi.org/10.1021/ma200952u.

[2] H. Nazaripoor, C.R. Koch, M. Sadrzadeh, S. Bhattacharjee, Thermo-electrohydrodynamic patterning in nanofilms, Langmuir 32 (23) (2016) 5776–5786, https://doi.org/10.1021/acs.langmuir.6b01810.

[3] H. Nazaripoor, C.R. Koch, M. Sadrzadeh, Enhanced electrically induced micropatterning of confined thin liquid films: thermocapillary role and its limitations, Ind. Eng. Chem. Res. 56 (38) (2017) 10678–10688, https://doi.org/10.1021/acs.iecr.7b02814.

[4] N. Wu, W.B. Russel, Micro- and nano-patterns created via electrohydrodynamic instabilities, Nano Today 4 (2) (2009) 180–192, https://doi.org/10.1016/j.nantod.2009.02.002. <http://www.sciencedirect.com/science/article/pii/S1748013209000048>.

[5] R. Mukherjee, A. Sharma, Instability, self-organization and pattern formation in thin soft films, Soft Matt. 11 (45) (2015) 8717–8740.

[6] N. Bhandaru, A. Sharma, R. Mukherjee, Programmable nanopatterns by controlled debonding of soft elastic films, ACS Appl. Mater. Interfaces 9 (23) (2017) 19409–19416, https://doi.org/10.1021/acsami.6b09127. pMID: 28610425.

[7] J.P. Singer, Thermocapillary approaches to the deliberate patterning of polymers, J. Polym. Sci., Part B: Polym. Phys. (2017) n/a–n/a, https://doi.org/10.1002/polb.24298.

[8] Y. Xia, G.M. Whitesides, Soft lithography, Annu. Rev. Mater. Sci. 28 (1) (1998) 153–184, https://doi.org/10.1146/annurev.matsci.28.1.153.

[9] J.A. Rogers, R.G. Nuzzo, Recent progress in soft lithography, Mater. Today 8 (2) (2005) 50–56, https://doi.org/10.1016/S1369-7021(05)00702-9. <http://www.sciencedirect.com/science/article/pii/S1369702105007029>.

[10] N. Bhandaru, P.S. Goohpattader, D. Faruqui, R. Mukherjee, A. Sharma, Solvent-vapor-assisted dewetting of prepatterned thin polymer films: control of morphology, order, and pattern miniaturization, Langmuir 31 (10) (2015) 3203–3214, https://doi.org/10.1021/la5045738. pMID: 25692553.

[11] E. Schaffer, T. Thurn-Albrecht, T.P. Russell, U. Steiner, Electrically induced structure formation and pattern transfer, Nature 403 (2000) 874–877, https://doi.org/10.1038/35002540.

[12] S.Y. Chou, L. Zhuang, L. Guo, Lithographically induced self-construction of polymer microstructures for resistless patterning, Appl. Phys. Lett. 75 (7) (1999) 1004–1006, https://doi.org/10.1063/1.124579.

[13] E. Schaffer, S. Harkema, M. Roerdink, R. Blossey, U. Steiner, Thermomechanical lithography: pattern replication using a temperature gradient driven instability, Adv. Mater. 15 (6) (2003) 514–517.

[14] M. Dietzel, S.M. Troian, Formation of nanopillar arrays in ultrathin viscous films: the critical role of thermocapillary stresses, Phys. Rev. Lett. 103 (2009) 074501, https://doi.org/10.1103/PhysRevLett.103.074501.

[15] E. McLeod, Y. Liu, S.M. Troian, Experimental verification of the formation mechanism for pillar arrays in nanofilms subject to large thermal gradients, Phys. Rev. Lett. 106 (17) (2011) 175501.

[16] L.D. Landau, E.M. Lifshitz, Electrodynamics of Continuous Media, Pergamon Press, 1960.

[17] L.F. Pease III, W.B. Russel, Electrostatically induced submicron patterning of thin perfect and leaky dielectric films: a generalized linear stability analysis, J. Chem. Phys. 118 (8) (2003) 3790–3803.

[18] R.V. Craster, O.K. Matar, Electrically induced pattern formation in thin leaky dielectric films, Physi. Fluids (1994-present) 17 (3) (2005) 1131–1198, https://doi.org/10.1063/1.1852459.

[19] H. Nazaripoor, C.R. Koch, M. Sadrzadeh, S. Bhattacharjee, Electrohydrodynamic patterning of ultra-thin ionic liquid films, Soft Matt. 11 (2015) 2193–2202, https://doi.org/10.1039/C4SM02477J.

[20] K. Mondal, P. Kumar, D. Bandyopadhyay, Electric field induced instabilities of thin leaky bilayers: pathways to unique morphologies and miniaturization, J. Chem. Phys. 138 (2) (2013) 024705, https://doi.org/10.1063/1.4773857. <http://link.aip.org/link/?JCP/138/024705/1>.

[21] H. Nazaripoor, C.R. Koch, S. Bhattacharjee, Electrical perturbations of ultrathin bilayers: role of ionic conductive layer, Langmuir 30 (49) (2014) 14734–14744, https://doi.org/10.1021/la503839x.

[22] N. Wu, L. Pease, W. Russel, Toward large-scale alignment of electrohydrodynamic patterning of thin polymer films, Adv. Funct. Mater. 16 (15) (2006) 1992–1999, https://doi.org/10.1002/adfm.200600092.

[23] A. Atta, D.G. Crawford, C.R. Koch, S. Bhattacharjee, Influence of electrostatic and chemical heterogeneity on the electric-field-induced destabilization of thin liquid films, Langmuir 27 (20) (2011) 12472–12485, https://doi.org/10.1021/la202759j. arXiv: <http://pubs.acs.org/doi/pdf/10.1021/la202759>.

[24] Q. Yang, B.Q. Li, H. Tian, X. Li, J. Shao, X. Chen, F. Xu, Deformation hysteresis of electrohydrodynamic patterning on a thin polymer film, ACS Appl. Mater. Interfaces 8 (27) (2016) 17668–17675, https://doi.org/10.1021/acsami.6b04192. pMID: 27326791.

[25] S. Dwivedi, Vivek, R. Mukherjee, A. Atta, Formation and control of secondary nanostructures in electro-hydrodynamic patterning of ultra-thin films, Thin Solid Films 642 (2017) 241–251, https://doi.org/10.1016/j.tsf.2017.09.029. <http://www.sciencedirect.com/science/article/pii/S0040609017306983>.

[26] L.F. Pease, W.B. Russel, Limitations on length scales for electrostatically induced submicrometer pillars and holes, Langmuir 20 (3) (2004) 795–804, https://doi.org/10.1021/la035022o. pMID: 15773107.

[27] H. Hu, H. Tian, X. Li, J. Shao, Y. Ding, H. Liu, N. An, Biomimetic mushroom-shaped microfibers for dry adhesives by electrically induced polymer deformation, ACS Appl. Mater. Interfaces 6 (16) (2014) 14167–14173, https://doi.org/10.1021/am503493u.

[28] H. Hu, H. Tian, J. Shao, Y. Ding, C. Jiang, H. Liu, Fabrication of bifocal microlens arrays based on controlled electrohydrodynamic reflowing of pre-patterned polymer, J. Micromech. Microeng. 24 (9) (2014) 095027. <http://stacks.iop.org/0960-1317/24/i=9/a=095027>.

[29] G. Liu, W. Yu, H. Li, J. Gao, D. Flynn, R.W. Kay, S. Cargill, C. Tonry, M.K. Patel, C. Bailey, M.P.Y. Desmulliez, Microstructure formation in a thick polymer by electrostatic-induced lithography, J. Micromech. Microeng. 23 (3) (2013) 035018. <http://stacks.iop.org/0960-1317/23/i=3/a=035018>.

[30] H. Tian, J. Shao, Y. Ding, X. Li, H. Hu, Electrohydrodynamic micro-/nanostructuring processes based on prepatterned polymer and prepatterned template, Macromolecules 47 (4) (2014) 1433–1438, https://doi.org/10.1021/ma402456u.

[31] S.H. Davis, Thermocapillary instabilities, Annu. Rev. Fluid Mech. 19 (1) (1987) 403–435, https://doi.org/10.1146/annurev.fl.19.010187.002155.

[32] A. Oron, S.H. Davis, S.G. Bankoff, Long-scale evolution of thin liquid films, Rev. Mod. Physi. 69 (1997) 931–980, https://doi.org/10.1103/RevModPhys.69.931.

[33] R.D. McCammon, R.G. Saba, R.N. Work, Dielectric properties of polystyrene and some polychlorostyrenes from 4k to room temperature, J. Polym. Sci. Part A-2: Polym. Phys. 7 (10) (1969) 1721–1733, https://doi.org/10.1002/pol.1969.160071008. arXiv: <https://onlinelibrary.wiley.com/doi/pdf/10.1002/pol.1969.160071008>.

[34] V.K. Thakur, D. Vennerberg, S.A. Madbouly, M.R. Kessler, Bio-inspired green surface functionalization of pmma for multifunctional capacitors, RSC Adv. 4 (2014) 6677–6684, https://doi.org/10.1039/C3RA46592F.

[35] J.N. Israelachvili, Intermolecular and Surface Forces, Academic Press, Burlington, MA, 2011. <http://login.ezproxy.library.ualberta.ca/login?url=http://search.ebscohost.com/login.aspx?direct=true&db=cat00362a&AN=neos.4932099&site=eds-live&scope=site>.

[36] E. schaffer, T. Thurn-Albrecht, T.P. Russell, U. Steiner, Electrohydrodynamic instabilities in polymer films, EPL (Europhys. Lett.) 53 (4) (2001) 518.

[37] E. Schaffer, S. Harkema, M. Roerdink, R. Blossey, U. Steiner, Morphological instability of a confined polymer film in a thermal gradients, Macromolecules 36 (5) (2003) 1645–1655, https://doi.org/10.1021/ma021080p. arXiv: <http://pubs.acs.org/doi/pdf/10.1021/ma021080>.

[38] J.P. Burelbach, S.G. Bankoff, S.H. Davis, Nonlinear stability of evaporating/condensing liquid films, J. Fluid Mech. 195 (1988) 463–494, https://doi.org/10.1017/S0022112088002484. <http://journals.cambridge.org/article_S0022112088002484>.

[39] R. Verma, A. Sharma, K. Kargupta, J. Bhaumik, Electric field induced instability and pattern formation in thin liquid films, Langmuir 21 (8) (2005) 3710–3721, https://doi.org/10.1021/la0472100. arXiv: http://pubs.acs.org/doi/pdf/10.1021/la047210.

[40] K.E. Brenan, L.R. Petzold, The numerical solution of higher index differential/algebraic equations by implicit methods, SIAM J. Numerical Anal. 26 (4) (1989) 976–996.

[41] N. Wu, W.B. Russel, Electrohydrodynamic instability of dielectric bilayers: kinetics and thermodynamics, Ind. Eng. Chem. Res. 45 (16) (2006) 5455–5465, https://doi.org/10.1021/ie0510876. arXiv: http://pubs.acs.org/doi/pdf/10.1021/ie051087.

[42] H. Nazaripoor, C.R. Koch, M. Sadrzadeh, S. Bhattacharjee, Compact micro/nano electrohydrodynamic patterning: using a thin conductive film and a patterned template, Soft Matt. 12 (2016) 1074–1084, https://doi.org/10.1039/C5SM02258D.